NANO LETTERS

2007
Vol. 7, No. 8
2540−2544

Synthesis of Single-Crystalline Zn Metal Nanowires Utilizing Cold-Wall Physical Vapor Deposition

Michael Kast,*,† Philipp Schroeder,† Youn J. Hyun,‡ Peter Pongratz,§ and Hubert Brückl†

Austrian Research Centers GmbH − ARC, Tech Gate Vienna, Donau-City-Strasse 1, A-1220 Vienna, Austria, and Vienna University of Technology, Karlsplatz 13, A-1040 Vienna, Austria

Received April 20, 2007; Revised Manuscript Received June 13, 2007

ABSTRACT

Zinc metal nanowires (NWs) of two different morphologies have been synthesized in a cold-wall physical vapor deposition (CWPVD) chamber at high vacuum conditions and growth temperatures of 150 °C. Substrates initially seeded by gold or platinum crystals show NWs of wool-like and/or unidirectional morphologies. Transmission electron microscopy (TEM) studies revealed that the rodlike NWs consist of single-crystalline Zn covered with a thin native oxide. NWs of wool-like morphology are suppressed using platinum as the seed metal. NW growth proceeds via vapor−solid (VS) kinetics without any catalyst particles on the wire tips. The highest observed growth rates exceed the Zn deposition rate by factors up to 860, indicating the dominant role of surface diffusion of Zn adatoms, also along the NWs. The surface diffusion length of Zn adatoms on the NW side facet is determined to be 39 μm. Direct impingement of precursor atoms on the NW tip is not significant for the growth process.

In the past decade, one-dimensional (1D) nanostructures such as NWs, nanotubes, or nanobelts gained significant importance as promising building blocks for the development of novel devices at the nanoscale. Among all growth techniques, those employing vapor transport methods and vapor−liquid−solid[1−3] (VLS) or vapor−solid[4] (VS) growth processes have been proven to be the most versatile regarding the composition and morphology of 1D nanostructures and the capability to self-assemble NW-enabled devices.[5] Many different materials including elemental and compound semiconductors, oxides, carbides, and nitrides were successfully synthesized utilizing such growth techniques. In the vapor−liquid−solid (VLS) process, the precursor vapor is dissolved in a liquid nanosized catalyst droplet until it reaches the state of supersaturation. The precursor material then precipitates continuously at the interface between the droplet and the substrate, thus forming wires of nanoscale diameters. In the vapor−solid (VS) process, crystallization along one direction is guided by anisotropy of crystal surface energies. During the growth process, the morphology of the NWs strongly depends on the complex interplay of the relevant parameters (ambient pressure, substrate temperature, etc.), which control the kinetics of precursor atoms on the substrate surface and on the NWs.

Metal NWs, which are considered as possible interconnects or functional elements in future nanodevices, need to be synthesized by alternative methods owing to the lack of applicable catalyst materials. The first metal NWs, which showed conductance quantization and ballistic transport, were fabricated by mechanical methods,[6−11] for example, by vertical pulling of scanning tunneling microscope tips after point contact.[6,7] Metal NWs were also fabricated by electrochemical thinning of microscale wires[12] and template-directed electrodeposition into nanoporous materials[13] (e.g., porous anodic alumina, track-etched polycarbonate, mesoporous silica, etc.). The resulting nanocomposites have well-defined geometries preset by the pore dimensions and granular, polycrystalline, or amorphous structures. Recently, single-crystalline NWs were demonstrated utilizing pulsed electrodeposition.[14] Electrochemical methods produce low yields due to the small template sizes. Postsynthesis device assembly may require removal of the nanoporous membrane which may cause damage to the NWs. Finally, metal NWs have also been demonstrated by step edge decoration[15] and solution phase methods.[16]

In this work, we present a cold-wall physical vapor deposition (CWPVD) chamber for the synthesis of metallic Zn nanowires. Zn nanocomposites have recently shown

* To whom correspondence should be addressed. E-mail: michael.kast@arcs.ac.at.
† Division Nano-System-Technologies.
‡ Solid State Electronics Institute, Floragasse 7, A-1040 Vienna, Austria.
§ Institute for Solid State Physics, Wiedner Hauptstrasse 8/052, A-1040 Vienna, Austria.

10.1021/nl070934m CCC: $37.00
Published on Web 07/11/2007

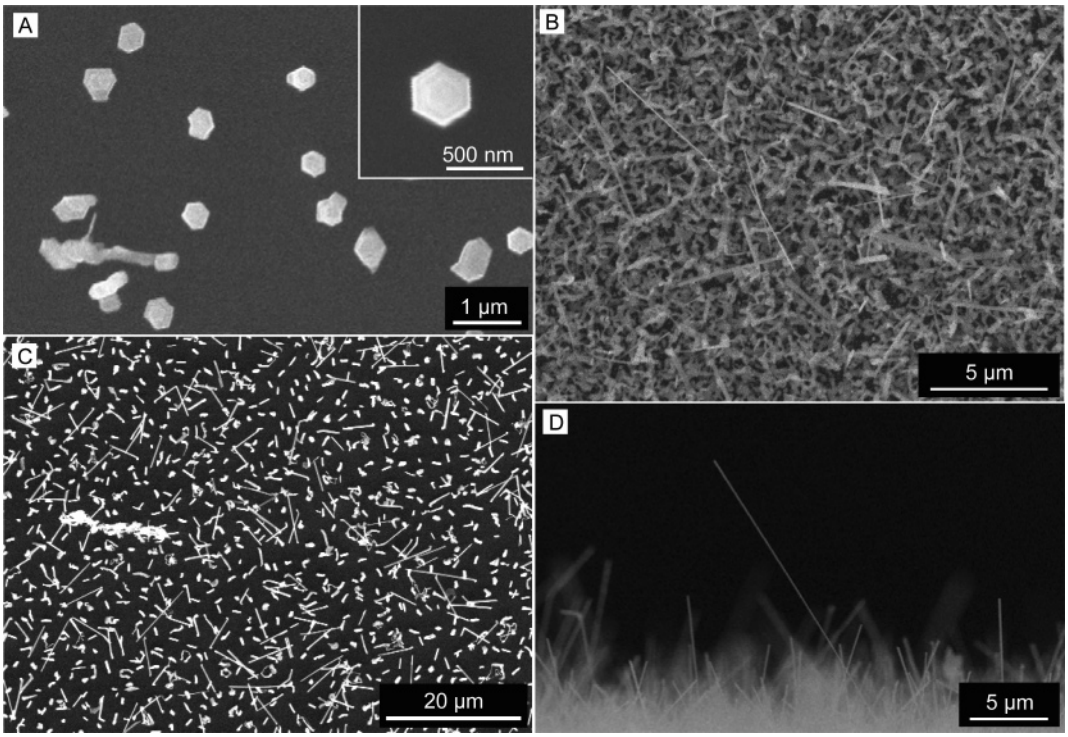

Figure 1. (A) Top-view SEM image of Zn nanocrystals grown on (100) silicon. (B) Top-view SEM image of wool-like and rodlike NWs grown on gold covered silicon surfaces at $T_s = 150$ °C. (C) Top-view SEM image of 1D NWs grown on platinum coated silicon surfaces at $T_s = 150$ °C. (D) Representative side-view SEM image of unidirectional NWs grown on the edges of gold or platinum coated silicon substrates. (Inset) SEM image of an individual hexagonal Zn nanocrystal.

unique thermoelectric and superconducting properties such as a very high room-temperature Seebeck coefficient[17] and a novel antiproximity effect in a system of electrodeposited Zn NW arrays sandwiched between superconducting bulk electrodes.[18] However, only a few groups focus on the synthesis of elemental Zn NWs by utilizing electrodeposition[18] or vapor transport methods: Vivekchand et al.[19] utilized a nebulized spray pyrolysis technique to synthesize wool-like Zn NWs by decomposition of Zn acetates at temperatures of 800−1000 °C. Kar et al.[20] synthesized similar structures by thermal evaporation of ZnS powders at 1225 °C. Besides the formation of ZnS nanoribbons, they also found wool-like Zn NWs in the cooler region of the quartz tube (∼350 °C). Synthesis of Zn NWs was also demonstrated by carbothermal reduction of ZnO with graphite at temperatures of 1100 °C[21] and 1060 °C.[22] Zn NWs were obtained by thermal evaporation of pure Zn at temperatures of 580 °C,[23] 600 °C,[24] and 900 °C[25]. The reported Zn NWs grow only in a wool-like morphology and are exclusively found in the cooler regions of the quartz tubes in an estimated temperature range of 200−350 °C.

It is apparent that the growth temperature in externally heated tube furnaces is strongly coupled to the sublimation temperature of the solid precursor materials. This coupling limits the parameter settings for NW synthesis. Therefore, we set up a CWPVD chamber in which the substrate temperature is controlled independently from the Zn vapor source. The chamber consists of standard vacuum parts. Elemental Zn (99.99%, Sigma-Aldrich) is thermally evaporated from an alumina crucible by resistive heating in high vacuum conditions. The sample is mounted on a distant heater facing down to the precursor vapor source. The temperature of the sample heater is measured by a type K thermocouple. A quartz microbalance (QMB) is used to monitor the Zn deposition rate and the nominal film thickness. The Zn atom flux to the substrate can be blanked by a mechanical shutter.

The (100)-Si wafers, which are cut into pieces of 2×2 cm^2, are prepared in different ways: we use (a) as-delivered Si wafers covered with native oxide and (b) HF etched substrates that are either bare or sputter coated with islandlike gold or platinum films (<3 nm). After the sample is mounted on the heater, the growth chamber is evacuated to base pressures of $\sim 5 \times 10^{-7}$ mbar. Subsequently, the work pressure is set within a range of 10^{-6}−10^{-5} mbar by introducing oxygen or argon gas into the growth chamber. The Zn evaporation rate is usually set to 0.1 nm/s, and the temperature is set to the growth temperature. The morphology and the composition of the as-grown NWs are analyzed by scanning electron microscopy (SEM, Philips XL40), energy dispersive X-ray analysis (EDX), and transmission electron microscopy (TEM, JEOL 200 CX; HRTEM, FEI Tecnai F-20).

Figure 1A shows a SEM image of Zn nanostructures grown on bare silicon without any metal seeds. At a substrate temperature of $T_s = 150$ °C, the evaporated Zn nucleates on the silicon surface and crystallizes in the hexagonal closed-packed lattice structure, assembling nanosized islands with the ⟨0001⟩ direction being perpendicular to the substrate surface. In contrast, Si substrates initially covered with gold seeds exhibit NWs of two different morphologies, as shown in Figure 1B ($T_s = 150$ °C). The dominating NWs have 1D

wool-like, also termed zigzag or serpentine, morphology, which has already been reported by other groups as mentioned above. In addition, rodlike NWs are also observed. A representative side view of NWs observed on the substrate surfaces and on the edges of the substrates is shown in Figure 1C. The NWs have diameters in the range of 30−350 nm and are up to 89 μm long. Figure 1D shows NWs grown on the substrate initially coated with platinum instead of gold at $T_s = 150$ °C. In contrast to the nanostructures obtained on the gold covered substrate, the surface does not show any wool-like NWs. The dominating NWs show rodlike morphology, are homogeneously distributed, and have uniform dimensions. They do not show any preferential growth direction. In between the NWs, the surface seems to be free of Zn deposits, indicating a high surface mobility of Zn adatoms. This observation is consistent with the growth on bare Si (Figure 1A). Furthermore, the Pt/Si substrates exhibit larger interwire spacings compared to the Au/Si substrates. Atomic force microscopy (AFM) measurements of Au/Si and Pt/Si surfaces prior to nanowire growth show similar high grain densities which imply that the density of the Zn nanowires on the individual substrate surfaces does not relate to the density of the metal seed (Pt or Au) islands or grains. In contrast, the metal seed layers (Pt or Au) modify the surface mobility of Zn on the Si substrate, hence resulting in different densities of critical Zn nuclei coalescing in the first stage of nanowire growth. AFM measurements also revealed a much lower surface roughness of Pt/Si substrates compared to that of Au/Si substrates. Increasing the surface roughness of Pt/Si by annealing the substrate prior to nanowire growth for 3 min at 650 °C leads to the same results as those obtained for Au/Si presented in Figure 1B. Therefore, we do not attribute the suppression of wool-like nanowires to the nature of the platinum seed material. We find that the growth of Zn nanowires on Si requires nanosized features which support Zn nucleation on the substrate surface. The density of the Zn nuclei depends on the Zn adatom surface mobility, which is influenced by the nanoscopic surface roughness. Therefore, smooth surfaces without pronounced nucleation sites favor the nucleation of homogeneous Zn nuclei which act as seeds for the growth of unidirectional nanowires.

Silicon substrates coated with 100 nm thick Au and Pt layers were also tested as samples for nanowire growth. After the individual growth runs, neither Zn grains nor Zn nanostructures could be observed on the metal surfaces. In addition, we evaporated Au layers exhibiting thickness gradients on silicon oxide using shadow masks. After nanowire growth, nanowires of rod- and wool-like morphologies are observed only in the areas where the Au coating becomes noncontinuous and islandlike. These formations of nanofeatures seem to act as nucleation sites. On continuous Au films, Zn obviously does not nucleate due to (i) the presence of metallic surface bonds which suppress surface diffusion in the first instance and (ii) probably alloy formation by bulk diffusion of Zn. On areas without Au, we observe Zn nanocrystals similar to the structures shown in Figure 1A. Zn island growth is favored due to the higher surface energy of Zn compared to that of SiO.

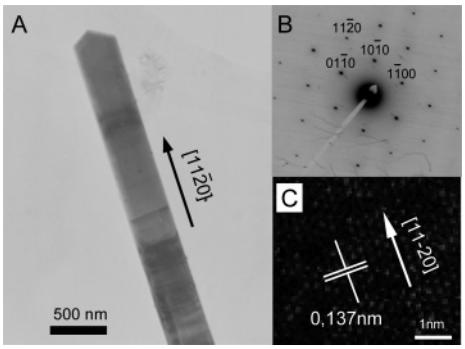

Figure 2. (A) Low magnification TEM image of a NW tip showing two distinct facets including an angle of 120°. (B) Diffraction pattern of a single-crystalline Zn NW. (C) HRTEM image of a Zn NW. The lattice plane distance of 0.137 nm determines the growth direction to be [11-20].

At growth temperatures higher than 200 °C, Zn does not nucleate on any of the aforementioned substrates. After the standard growth time of 1 h, the samples did not show any Zn deposits. A high Zn desorption rate at $T_s \geq 200$ °C dominates surface diffusion and hence impedes Zn nucleation on the sample surface. At this point, it is important to note that the morphologies of the Zn nanostructures grown by CWPVD do not depend on the type of gas used during the individual growth runs.

EDX measurements have proven that all nanostructures grown on the various substrates consist of pure Zn. Figure 2A shows a low magnification TEM image of an individual NW of rodlike morphology harvested from the substrate surface after an ultrasonic treatment and dispersed onto a copper grid. The NW tip shows two distinct facets including an angle of 120°. The diffraction pattern shown in Figure 2B reveals a single-crystalline phase. Figure 2C shows a high-resolution TEM (HRTEM) image of the Zn lattice planes perpendicular to the growth direction. From the lattice plane distance of 0.137 nm, we deduce the growth direction to be [11-20]. This growth direction was determined on all NWs studied, independent of the seed material. Figure 3A shows a HRTEM image of the NW sidewall. The dark area depicts the core of the NW consisting of single-crystalline Zn covered with a 2 nm thick native oxide (dark gray). The HRTEM image shown in Figure 3B reveals the single-crystallinity of the surface oxide.

Since no catalyst particles are present on the tips of the NWs, it is evident that the synthesis proceeds via the VS growth process: First, precursor atoms nucleate on the substrate surface, forming nanocrystallites. In a second stage, continuously adsorbing Zn adatoms migrate to the nanocrystallites being incorporated at positions having the lowest surface energies. If the nanocrystals form stable side facets, crystallization is driven along one direction, that is, [11-20] resulting in 1D NW growth. The ratio of the NW length growth rate to the precursor deposition rate is a first measure of the Zn adatom mobility on the NW. In our experiments, the highest NW length growth rate obtained from SEM analysis equals $R_{NW} = 53.33$ nm/s, which exceeds the

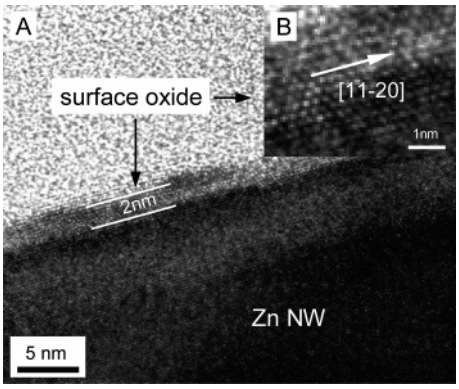

Figure 3. (A) HRTEM image of a Zn NW sidewall covered with a 2 nm thick surface oxide. (B) HRTEM image of a single-crystalline surface oxide.

deposition rate of $R_{Zn} = 0.062$ nm/s by a factor of 860. This remarkable result gives direct evidence that the NWs are predominantly formed by surface diffusing Zn adatoms and that direct impingement of precursor atoms on the NW tip does not play a significant role during the growth process.

The Zn surface diffusion length on the NW sidewall is determined using the mass transport model presented by Seifert et al.[26] In this model, a liquid catalyst particle on the NW tip acts as a sink which creates the driving force for material flow from the substrate surface and the NW sidewalls toward the NW tip. Effective surface diffusion lengths on the substrate λ_s and along the nanowire λ_w, which are obtained from studying the dependence of the NW length growth rate dL/dt on the NW radius r_w, are introduced. In the late-stage growth, where $L \gg \lambda_w$, the length growth rate is given by the simple equation $dL/dt = 2R(1 + \lambda_w/r_w)$, where R stands for the effective impingement rate of adatoms on the substrate surface, NW sidewalls, and NW tips. The first term on the right side depicts the growth by direct impingement of precursor atoms on the NW tip. The second term depicts diffusion controlled growth. The main conclusion of this equation is that thinner NWs grow faster than thicker ones. To apply this mass transport model to VS growth of Zn NWs, the hemispherical liquid catalyst particle is replaced by the cone-shaped tip shown in Figure 2A. In contrast to the initial model, where the full NW shell is exposed to impinging reactants, only half of the NW shell is exposed to the highly directed precursor deposition flux due to shadowing effects in high vacuum conditions. As a consequence, the NW length growth rate results in $R_{NW} = R_{Zn}(1.155 + \lambda_w/r_w)$. Since the ratio R_{NW}/R_{Zn} exceeds values of 850 as mentioned above, the contribution of direct impingement on the NW tip is neglected and the equation can be reduced to $\lambda_w = (R_{NW}/R_{Zn})r_w$. Since the growth of individual NWs starts randomly in time during one growth run, the NWs show a clear length distribution, as can be seen in Figure 1D. As a consequence, the geometry of the longest NW observed by SEM ($L = 89\ \mu$m, $r_w = 100$ nm, and $t = 60$ min) only allows determination of a lower limit of the effective surface diffusion length, which results in $\lambda_w \geq 39\ \mu$m.

The surface diffusion length plays a crucial role in how the NW lateral size develops during the growth process. In diffusion controlled NW growth processes, tapering of the NW diameter occurs at NW lengths exceeding the surface diffusion length.[27] Since most of our nanowires do not exceed this length, as shown in Figure 1C, we do not observe any tapered nanowires by SEM.

In summary, one-dimensional Zn NWs were synthesized in a CWPVD chamber at substrate temperatures of $T_s = 150$ °C. The resulting NWs show serpentine and/or unidirectional morphologies, depending on the seed material. The growth proceeds via vapor−solid kinetics, since no catalyst particles are present on the NW tips. TEM studies revealed that rodlike NWs consist of single-crystalline Zn covered with a thin native oxide. The growth direction of the Zn rods is determined to be [11-20]. The NW growth rate exceeds the Zn evaporation rate by a factor of 860, indicating that the NW is assembled by Zn adatoms diffusing on the substrate surface and on the NW sidewalls. A simple model has been introduced which allows determination of a lower limit of the surface diffusion length of Zn adatoms on the NW sidewall from the experimental results. In conclusion, a route to low-temperature synthesis of elemental Zn NWs utilizing CWPVD is successfully demonstrated.

References

(1) Wagner, R. S.; Ellis, W. C. *Appl. Phys. Lett.* **1964**, *4*, 89.
(2) (a) Ohlsson, B. J.; Magnusson, M. H.; Björk, M. T.; Wallenberg, L. R.; Deppert, K.; Samuelson, L. *Appl. Phys. Lett.* **2001**, *79*, 3335. (b) Björk, M. T.; Ohlsson, B. J.; Sass, T.; Persson, A. I.; Thelander, C.; Magnusson, M. H.; Deppert, K.; Wallenberg, L. R.; Samuelson, L. *Nano Lett.* **2002**, *2*, 87.
(3) (a) Lieber, C. M. *Solid State Commun.* **1998**, *107*, 607. (b) Cui, Y.; Lieber, C. M. *Science* **2001**, *291*, 851.
(4) (a) Wang, Z. L. *J. Phys.: Condens. Matter* **2004**, *16*, R829. (b) Wang, X.; Song, J.; Wang, Z. L. *Chem. Phys. Lett.* **2006**, *424*, 86. (c) Yang, R.; Chueh, Y.; Morber, J. R.; Snyder, R.; Chou, L.; Wang, Z. L. *Nano Lett.* **2007**, *7*, 269. (d) Lee, J. S.; Islam, M. S.; Kim, S. *Nano Lett.* **2006**, *6*, 1487.
(5) (a) Islam, M. S.; Sharma, S.; Kamins, T. I.; Williams, R. S. *Nanotechnology* **2004**, *15*, L5. (b) Kamins, T. I.; Sharma, S.; Yasseri, A. A.; Li, Z.; Straznicky, J. *Nanotechnology* **2006**, *17*, S291.
(6) Gimzewski, J. K.; Moller, R. *Phys. Rev. B* **1987**, *36*, 1284.
(7) (a) Pascual, J. I.; Mendez, J.; Gomez-Herrero, J.; Baro, A. M.; Garcia, N.; Binh, V. T. *Phys. Rev. Lett.* **1993**, *71*, 1852. (b) Pascual, J. I.; Mendez, J.; Gomez-Herrero, J.; Baro, A. M.; Garcia, N.; Landman, U.; Luedtke, W. D.; Bogachek, E. N.; Cheng, H. P. *Science* **1995**, *267*, 1793.
(8) (a) Muller, C. J.; van Ruitenbeek, J. M.; de Jongh, L. J. *Phys. Rev. Lett.* **1992**, *69*, 140. (b) Krans, J. M.; van Ruitenbeek, J. M.; Fisun, V. V.; Yanson, I. K.; de Jongh, L. J. *Nature* **1995**, *375*, 767.
(9) Landman, U.; Luedtke, W. D.; Salisbury, B. E.; Whetten, R. L. *Phys. Rev. Lett.* **1996**, *77*, 1362.
(10) Costa-Kramer, J. L.; Garcia, N.; Garcia-Mochales, P.; Serena, P. A. *Surf. Sci.* **1995**, *342*, L1144.
(11) Yasuda, H.; Sakai, A. *Phys. Rev. B* **1997**, *56*, 1069.
(12) (a) Li, C. Z.; Tao, N. J. *Appl. Phys. Lett.* **1998**, *72*, 894. (b) Li, C. Z.; Bogozi, A.; Huang, W.; Tao, N. J. *Nanotechnology* **1999**, *10*, 221.
(13) (a) Elhoussine, F.; Matefi-Tempfli, S.; Encinas, A.; Piraux, L. *Appl. Phys. Lett.* **2002**, *81*, 1681. (b) Tian, M.; Wang, J.; Kurtz, J.; Mallouk, T. E.; Chan, M. H. W. *Nano Lett.* **2003**, *3*, 919.
(14) Li, L.; Yang, Y.; Huang, X.; Li, G.; Zhang, L. *Nanotechnology* **2006**, *17*, 1706.
(15) Himpsel, F. J.; Jung, T.; Ortega, J. E. *Surf. Rev. Lett.* **1997**, *4*, 371.
(16) Gates, B.; Yin, Y.; Xia, Y. *J. Am. Chem. Soc.* **2000**, *122*, 12582.
(17) Heremans, J. P.; Thrush, C. M.; Morelli, D. T.; Wu, M. C. *Phys. Rev. Lett.* **2003**, *91*, 76804.

(18) (a) Wang, J. G.; Tian, M.; Kumar, N.; Mallouk, T. E. *Nano Lett.* **2005**, *5*, 1247. (b) Tian, M.; Kumar, N.; Xu, S.; Wang, J.; Kurtz, J. S.; Chan, M. H. W. *Phys. Rev. Lett.* **2005**, *95*, 76802.
(19) Vivekchand, S. R. C.; Gundiah, G.; Govindaraj, A.; Rao, C. N. R. *Adv. Mater*. **2004**, *16*, 1842.
(20) Kar, S.; Ghoshal, T.; Chaudhuri, S. *Chem. Phys. Lett.* **2006**, *419*, 174.
(21) Yan, Y.; Liu, P.; Romero, M. J.; Al-Jassim, M. M. *J. Appl. Phys.* **2003**, *93*, 4807.
(22) Li, J.; Chen, X. *Solid State Commun.* **2004**, *131*, 769.
(23) Peng, X. S.; Zhang, L. D.; Meng, G. W.; Yuan, X. Y.; Lin, Y.; Tian, Y. T. *J. Phys. D: Appl. Phys.* **2003**, *36*, L35.
(24) Liu, J.; Zhang, Z.; Su, X.; Zhao, Y. *J. Phys. D: Appl. Phys.* **2005**, *38*, 1068.
(25) Wen, X.; Fang, Y.; Yang, S. *Angew. Chem., Int. Ed.* **2005**, *44*, 3562.
(26) (a) Seifert, W.; Borgström, M.; Deppert, K.; Dick, K. A.; Johansson, J.; Larsson, M. W.; Mårtensson, T.; Sköld, N.; Svensson, C. P. T.; Wacaser, B. A.; Wallenberg, L. R.; Samuelson, L. *J. Cryst. Growth* **2004**, *272*, 211. (b) Johansson, J.; Svensson, C. P. T.; Mårtensson, T.; Samuelson, L.; Seifert, W. *J. Phys. Chem. B* **2005**, *109*, 13567.
(27) Dubrovskii, V. G.; Sibirev, N. V.; Cirlin, G. E.; Harmand, J. C.; Ustinov, V. M. *Phys. Rev. E* **2006**, *73*, 21603.

NL070934M